JOURNAL OF CATALYSIS **173,** 409–422 (1998)
ARTICLE NO. CA971917

Electron Microscopy of Thin-Film Model Catalysts: Activation of Alumina-Supported Rhodium Nanoparticles

G. Rupprechter,*[,1] K. Hayek,* and H. Hofmeister†

*Institute of Physical Chemistry, Leopold Franzens University Innsbruck, A-6020 Innsbruck, Austria; and †Max Planck Institute of Microstructure Physics, D-06120 Halle/Saale, Germany

Received June 11, 1997; revised September 1, 1997; accepted September 11, 1997

Well-faceted polyhedral Rh nanocrystals, epitaxially grown on NaCl (001) and supported by amorphous alumina, were selected to study the effect of oxidation and reduction on particle microstructure and on catalytic properties. The crystal habit, surface structure, and surface composition of the crystallites were determined by high-resolution electron microscopy assisted by digital image processing and contrast simulation, by weak-beam dark-field imaging, and by selected area electron diffraction. Their catalytic performance in the hydrogenolysis of alkanes was tested by microreactor kinetics. In the as-prepared state most Rh crystallites had smooth, low-Miller-index bounding faces and exhibited a half-octahedral or half-tetrahedral shape. Because of their regular habit these particles represent a well-defined initial state in a study of activation-induced morphology changes. After oxidation at 575 K a thin surface oxide was evident, whereas oxidation at 725 K led to the oriented overgrowth of hexagonal α-Rh_2O_3 on Rh. Oxidation at 725 K followed by low-temperature reduction at 525 K produced Rh particles with disordered surfaces, e.g., polycrystalline Rh particles or sandwich structures of Rh and Rh_2O_3. However, when oxidation at 725 K was followed by high-temperature reduction at 725 K, the low-Miller-index facets were reestablished. High turnover frequencies were observed on catalysts containing mainly Rh particles with disordered ("rough") surfaces, whereas smooth close-packed facets dominated in less active catalysts. The results confirm that high-index faces (low-coordinated sites) are preferred for hydrogenolysis. © 1998 Academic Press

1. INTRODUCTION

To establish a correlation between the structure and the activity of supported metal catalysts is still a major challenge in heterogeneous catalysis. For that purpose, a detailed knowledge of the surface structure of the metal particles, in particular of their exposed facets, edges, corners, etc., in the activated state is indispensable. The activation, or rejuvenation, of oxide-supported noble metals generally comprises a sequence of oxidation (calcination) and reduction steps at elevated temperature and will result in thermally stable particles and in high and reproducible reaction rates. This treatment not only removes contaminants but also leads to distinct structural and morphological changes of the metal/oxide system as a whole. The growing evidence that the type of pretreatment has a major effect on the turnover frequency of catalysts has led Bond in a recent review (1) to stress the importance of a full control over activating processes.

Electron microscopy in connection with selected area electron diffraction (SAED) has been frequently used for catalyst characterization and it has proved to be a powerful method to monitor microstructural changes on heat treatments in different ambients. In industrial catalysts an unambiguous characterization of the active catalyst particles is generally prevented by the strong contrast originating from the support, as well as by the random orientation and by the irregular shape of the metal particles. Therefore, model catalyst systems, specifically model supports, such as thin planar oxide films (2–7), nonporous submicron oxide particles (8, 9), thin alumina films prepared by sol–gel techniques (10, 11), and low-surface-area supports (12), have been used in connection with electron microscopy for quite some time. The alterations observed after treatments in oxygen and hydrogen include faceting, sintering, and redispersion of the metal particles and, under special conditions, also their decoration by mobile suboxides (one possible explanation of the SMSI effect). The synthesis, characterization, and applications of a variety of model catalyst systems have recently been reviewed by Gunter *et al.* (13).

In the last decade studies of the morphology, microstructure, and surface composition of small metallic particles in supported catalysts have benefited from the introduction of high-resolution electron microscopy [HREM] (14, 15). Structural details can now be revealed at an atomic scale providing direct evidence for, e.g., surface reordering (16, 17) and metal–support interaction (18, 19). Unfortunately, lattice imaging by HREM, especially in the profile-imaging mode, is restricted to particular orientations of the

[1] To whom correspondence should be addressed. Present address: Department of Chemistry, University of California at Berkeley, D54 Hildebrand Hall, Berkeley, CA 94720-1460.

0021-9517/98 $25.00

particles and of their surfaces; i.e., a low-index zone axis and the surface of interest have to be aligned parallel to the incident electron beam. The application of the method in a study of randomly oriented metal particles is therefore limited (with the exception of tilt experiments), but this restriction can be overcome by the use of epitaxially grown and well-oriented metal films.

In an earlier communication (20) we described the preparation and properties of oriented thin-film model catalysts of Pt, Rh, Ir, and Pd on Al_2O_3. Well-faceted noble metal nanocrystals are grown epitaxially on NaCl substrates and subsequently embedded in the supporting oxide. The metal/oxide films are finally removed from the substrate by flotation. After preparation for electron microscopy most metal particles exhibit [001] or [011] zone axes parallel to the beam direction and are therefore well suited for lattice plane imaging. Because of their alignment, their characterization by SAED and by weak-beam dark-field imaging is also considerably facilitated. The regular habit of the as-grown metal nanocrystals provides a definite "initial state," a starting point to understand the microstructural changes during the following activation or regeneration or during a catalytic reaction. Moreover, metal particles grown epitaxially on large-area NaCl films provide enough surface area for kinetic measurements in a microreactor (21–24).

In this paper we present a comprehensive study of the structural alterations of epitaxially grown rhodium particles embedded in a film of a nonreducible oxide (amorphous alumina) on moderate oxidative and reductive activating treatments; i.e., both oxidation and reduction occur at temperatures below about 725 K.

Like any other freshly prepared catalyst, the epitaxial model catalyst films exhibit only very low catalytic activity in the as-grown state. For the Rh/Al_2O_3 system, oxidation at 675–725 K followed by low-temperature reduction at 525 K (LTR) has proved to result in an activity maximum and in reproducible turnover rates in various reactions of H_2 with hydrocarbons. For instance, in the hydrogenolysis of neopentane at 475 K (10–50 mbar neopentane, 50–500 mbar H_2) intitial turnover frequencies of about 100 h^{-1} were observed (25, 26). On the other hand, if the oxidation is followed by high-temperature reduction in H_2 ($T \sim 725$ K, HTR) a fivefold decrease in turnover rate is evident.

A survey of recent reports shows that general agreement exists on the influence of these different pretreatments on the catalytic performance of supported Rh. However, it also reveals that many questions concerning the effect of annealing in various oxidizing or reducing ambients on the structure of the individual particles on different supports remain unanswered.

Schmidt and co-workers (27–30) explained the increased activity of supported Rh after oxidation at 775 K followed by LTR by the breakup of large (>10 nm) particles into smaller (>1 nm) ones, i.e., by an intraparticle redispersion producing low-coordinated sites. On reduction at higher temperature the small metal particles are again subject to sintering and this leads to a reduction in activity. In contrast, Datye *et al.* (31–35) observed a restructuring of the particle surface of Rh/SiO_2 under comparable conditions without any particle breakup (but with similar kinetic effects). Preoxidation followed by LTR resulted in the formation of polycrystalline aggregates with rough surfaces, whereas HTR led to the recrystallization into single-crystal particles. The experimental disagreement between the two systems may be due to the different methods of support preparation (planar thin films vs nonporous submicrometer silica spheres). Also, the nature of the Rh-oxide phases formed during the progressive oxidation is still under debate. For these reasons a detailed analysis of the microstructural changes of our particular model system on activation seems necessary and worthwhile. In a forthcoming paper (26) a structure–activity correlation in the hydrogenolysis of methylcyclobutane and neopentane on Rh/Al_2O_3 and Rh/TiO_2 is tentatively established based in part on the results of the present microstructural investigation.

2. METHODS

Two types of NaCl substrates were used for the preparation of well-shaped metal particles: vacuum-cleaved NaCl (001) single-crystal faces (0.25 cm^2) and *in situ* deposited NaCl films (up to 100 cm^2; prepared by NaCl evaporation on Cu sheets at 360 K) (20). The structure of the metal particles is identical on both types of substrates [except for some marginal particle coalescence at the grain boundaries in the NaCl films (36)]. The specimens grown on the NaCl films provide sufficient area for kinetic measurements and are described elsewhere (26).

The Rh/Al_2O_3 films were prepared in a high-vacuum chamber at a base pressure of 1×10^{-5} Pa. Nanosize Rh particles of well-defined shape were grown on NaCl (001) single-crystal faces by physical vapor deposition at substrate temperatures between 600 and 650 K. The NaCl single crystals were cleaved *in vacuo* immediately before the metal condensation. Rh was evaporated by electron bombardment of the tip of a pure Rh rod. The impinging flux was 1.2×10^{13} atoms cm^{-2} s^{-1} (0.1 nm min^{-1}) and the nominal film thickness was 0.8 nm in all the present experiments (monitored by a quartz crystal oscillator). Thereafter, the samples were cooled to room temperature *in vacuo* and covered with 25 nm of amorphous Al_2O_3 by reactive evaporation of Al in an atmosphere of 10^{-2} Pa O_2 at a growth rate of 1 nm min^{-1} (Al was evaporated from a resistively heated Ta filament). The resulting metal/oxide films were removed from the NaCl substrate by flotation, carefully rinsed in water, and mounted on gold grids for electron microscopy (EM) examination.

Several EM techniques were applied to determine the morphology and microstructure of the model catalysts: Conventional transmission electron microscopy (CTEM), SAED, weak-beam dark-field (WBDF) imaging (Zeiss EM 10C and Jeol 100C operated at 100 kV), and HREM (Jeol 4000 EX operated at 400 kV).

An elemental analysis of rather thick Rh and Al_2O_3 films (up to 0.5 μm) was made by energy-dispersive X-ray fluorescence (XRF; Oxford XR400) and electron probe X-ray microanalysis (EPMA; ARL) to ensure that no traces of source materials or impurities were present (the detection limit of XRF is approx 200 ppm).

The conventional transmission electron micrographs were subjected to digital image processing for contrast enhancement and quantitative image evaluation (analysis of mean particle diameter, crystallite number density, and metal coverage). To determine lattice spacings and angles between atomic planes fast Fourier transforms (FFTs) of digitized HREM images of individual particles were used. Frequency domain (power spectrum) filter operations were applied to reveal fine details in HREM images, e.g., by suppression of contrast originating from the support (software Image ProPlus by Media Cybernetics and NIH Image by Wayne Rasband).

For activation the specimens were transferred to a microreactor (24). Traces of atmospheric water were removed by heating *in vacuo* at 400 K and the specimens were then annealed in 1 bar of oxygen or hydrogen between 475 and 800 K for a given time (heating rate 60 K min^{-1}). Between oxygen and hydrogen treatments the samples were cooled rapidly (cooling rate 30 K min^{-1}) and then evacuated and purged several times with helium.

3. RESULTS

3.1. Habit, Orientation, and Surface Structure of As-Grown Rh Particles

A variety of different polyhedral Rh particles were observed in epitaxially grown Rh/Al_2O_3 model catalysts. Depending on the substrate temperature, the number density of particles varied between 3.5×10^{11} cm^{-2} at 600 K and 1.5×10^{11} cm^{-2} at 650 K. The corresponding mean particle sizes were approximately 4 and 9 nm (nominal film thickness, 0.8 nm). CTEM images in the bright- and dark-field modes and HREM micrographs were essential to analyze the crystal habit and the orientation of the Rh particles (Figs. 1 and 2). To enhance the visibility of image details like particle edges and corners, surface steps, or the metal–support boundary, digitized HREM images were Fourier transformed and spatial frequencies originating from the support were partly suppressed (Fig. 2) (15). Bragg masks with smooth edges of Gaussian transition type were used to separate the metal FFT spots from the background (and are shown in Fig. 2b).

A survey of the various particle profiles is presented in Fig. 1a and some particles with square (s), pentagonal (p and pp), triangular (t), rhombic (r), and hexagonal (h) outlines

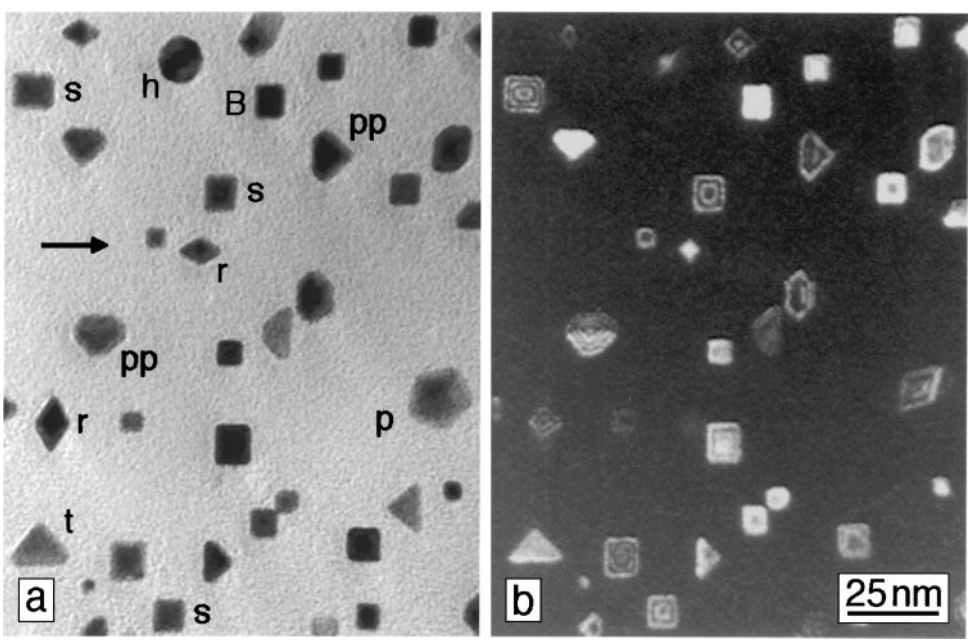

FIG. 1. (a) Bright-field and (b) (200) weak-beam dark-field images of epitaxially grown Rh model catalyst particles supported by amorphous Al_2O_3. Some nanocrystals with square, pseudopentagonal, triangular, rhombic, pentagonal, and hexagonal outlines are indicated [the arrow denotes the [110] direction of the former substrate NaCl].

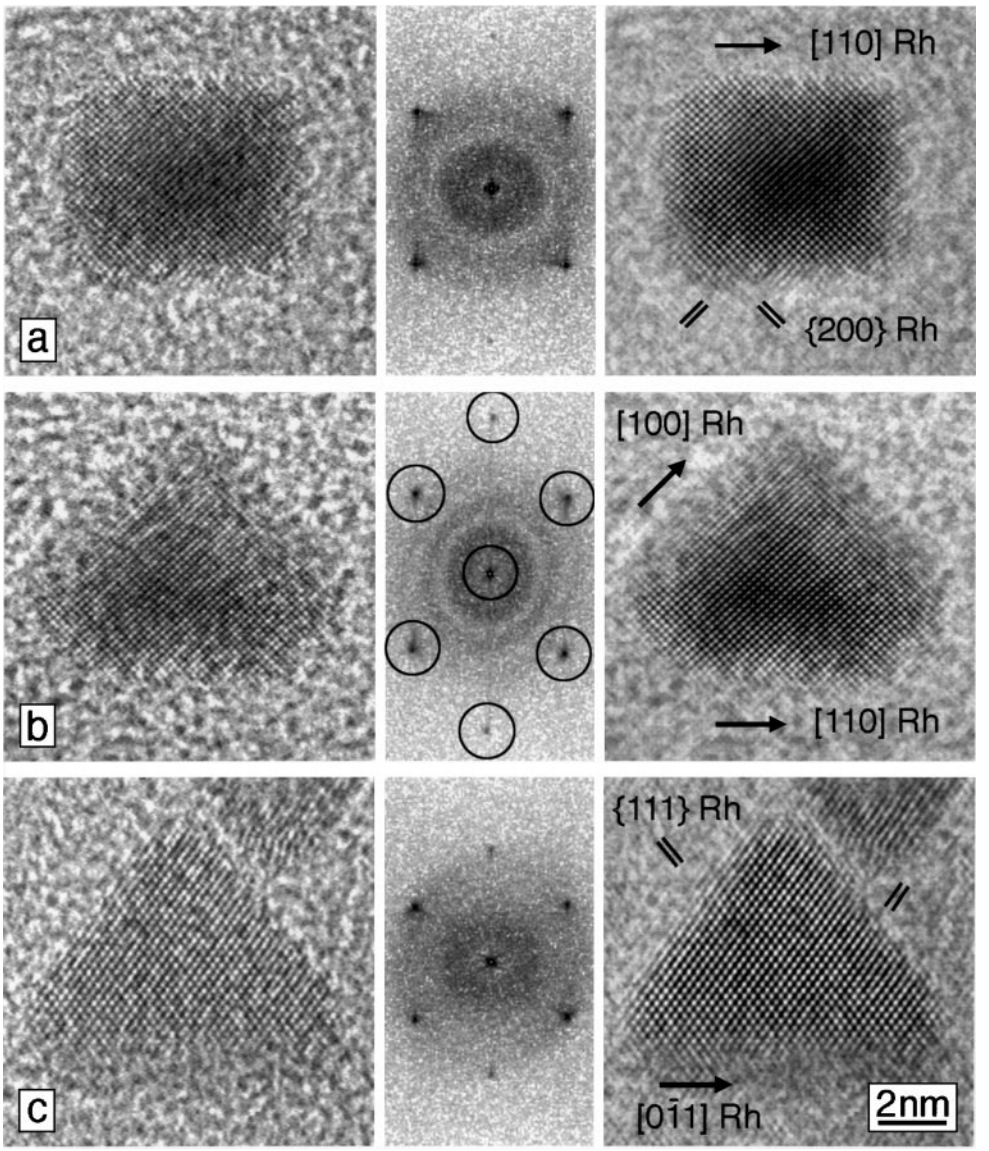

FIG. 2. High-resolution electron micrographs of a (001)-oriented half-octahedron (a), a (001)-oriented pseudopentagonal pyramid (b), and a (011)-oriented half-tetrahedron (c). Left: experimental images; center: FFTs; right: processed images after background suppression by Fourier filtering [Bragg masks are shown in (b); see text].

are indicated. In Fig. 1b the corresponding WBDF image is shown (the selected spots of the electron diffraction pattern are marked in Fig. 8a). Dark-field images of particles slightly deviating from the Bragg position appear with equithickness fringes (i.e., height contours) and from the fringe structure and fringe spacings topographical information can be obtained (the tilt angles were approx 4°) (15). Due to a slight bending of the supporting film caused by the preparation for electron microscopy, particles in Bragg position (denoted B in Fig. 1a) and particles tilted away from the Bragg condition are imaged simultaneously. High-resolution electron micrographs of the most abundant particles are shown in Fig. 2 together with their FFTs and Fourier-filtered images.

Approximately 80% of the metal particles exhibited strictly square or slightly rectangular outlines, e.g., particles s in Fig. 1a (the selected specimen position displays particles of all different shapes together). High-resolution electron micrographs of the square particles showed two sets of {200} lattice plane fringes (interplanar distance 0.190 nm), indicating a (001) orientation and an edge direction of ⟨110⟩ (Fig. 2a). Their orientation is also illustrated by the FFT of the particle shown in Fig. 2a which can be indexed like a microdiffraction pattern (15, 37). The crystal habit of s-type particles as determined by WBDF imaging is a half-octahedron with a (001) base plane and four {111} side faces (Fig. 1b, see also Fig. 7a). While extended (001) truncations

at the top (parallel to the base) or distinct {110} truncations at the corners have frequently been observed on (half)-octahedral Pt, Pd, and Au particles (38–40), such deviations from the regular shape were only very infrequently detected for Rh. The epitaxial orientation of the half-octahedra with respect to the substrate NaCl, as deduced from the decoration of ⟨100⟩ substrate steps, is (001) Rh ‖ (001) NaCl, [110] Rh ‖ [110] NaCl. The NaCl [110] direction is indicated in Fig. 1a by an arrow.

Figure 2b is the HREM image of a particle with a pentagonal profile (particles pp in Fig. 1a). Although the lattice fringe structure and FFT and, therefore, the orientation are equal to those of the half-octahedron in Fig. 1a, it should be noted that the edge directions are different. Only one edge is aligned along ⟨110⟩; four edges have a ⟨100⟩ direction. According to the WBDF images in Fig. 1b these particles are pseudopentagonal pyramids with a (001) base and one {111} and four {110} side faces. They should not be confused with the multiply twinned pentagonal particles p, which will be described below. pp particles may adopt an almost triangular profile in low-magnification images because two of the ⟨100⟩ edges are generally small. In addition, (001) truncations at the top may appear. Due to their reduced symmetry these particles grow on NaCl (001) in four equivalent azimuthal alignments with 90° rotation with respect to each other.

A crystallite with a (true) triangular profile is presented in Fig. 2c (see also particle t in Fig. 1a). The HREM image and the FFT reveal two families of {111} lattice plane fringes (interplanar distance 0.220 nm) and indicate a (011) orientation of the particle. According to dark-field microscopy these particles are half-tetrahedra with a (011) base plane and three {111} side faces (20). The edges, respectively the corners, of the half-tetrahedra may be truncated by small {100} and {111} facets. WBDF imaging shows that truncations parallel to the base are frequent; i.e., these particles may adopt the shape of flat platelets (resulting in uniform contrast in dark field). The half-tetrahedra appear in two azimuthal orientations rotated by 90°, i.e., (011) Rh ‖ (001) NaCl, [0$\bar{1}$1] Rh ‖ [110] NaCl or [1$\bar{1}$0] NaCl, and two equivalent twin-related positions are found for each (011) orientation [double positioning (41)].

Rh particles with rhombic, pentagonal, and hexagonal profiles (r, p, and h in Fig. 1a) appear as a small fraction (<10%) and are mentioned here only briefly because a detailed HREM characterization has been given earlier (42). They are multiply twinned particles (MTPs) such as decahedra in a (001) edge orientation (r), in a (011) fivefold axis orientation, and in a (111) face orientation (p), or as icosahedra in a (112) edge orientation (h). Typically, some of the twin-related tetrahedral building units are imaged in dark field (40, 43), e.g., the base tetrahedron of the (001) decahedra (r) and two of the five tetrahedra of particle p. Like the pseudopentagonal pyramids and the half-tetrahedra, the MTPs were also observed in different azimuthal orientations. Depending on the azimuthal alignment of the (001) base tetrahedron of particles r, their longitudinal axis may be directed either along [110] or along [1$\bar{1}$0] NaCl. Two preferred azimuthal orientations of the base tetrahedron were observed for the decahedra in face orientation (p), i.e., (111) Rh ‖ (001) NaCl, [1$\bar{1}$0] Rh ‖ [100] NaCl or [010] NaCl. The longitudinal axis of the two top tetrahedra is therefore preferentially aligned along ⟨100⟩ NaCl. Similarly to the half-tetrahedra, the (111) decahedra appear also in double positioning.

To summarize all the information about the orientation and azimuthal alignment of the various Rh nanoparticles, a schematic representation of the different diffraction patterns is given in Fig. 3 for each type of particle, together with the crystallographic axes of the original substrate NaCl. Only the most intense reflections are taken into account and icosahedral particles are not included due to their small proportion [their {111} reflections correspond to those of the decahedra; for diffraction patterns of MTPs see (43)]. The good agreement between the experimental SAED pattern (Fig. 8a) and the diffraction pattern in Fig. 3a formed

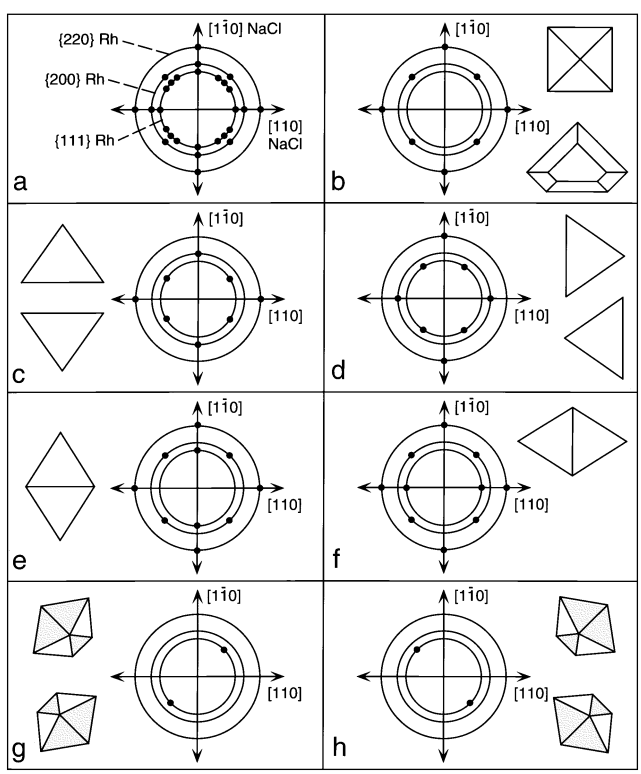

FIG. 3. (a) Schematic representation of the electron diffraction pattern of Rh/Al_2O_3 model catalysts. Rh {111}, {200}, and {220} reflections are shown together with the ⟨110⟩ directions of the NaCl substrate. The SAED pattern in (a) represents a superposition of the contributions (b–h) of the different types of epitaxial particles: (b) (001) half-octahedra and pseudopentagonal pyramids; (c, d) (011) half-tetrahedra; (e, f) (001) decahedra; (g, h) (111) decahedra.

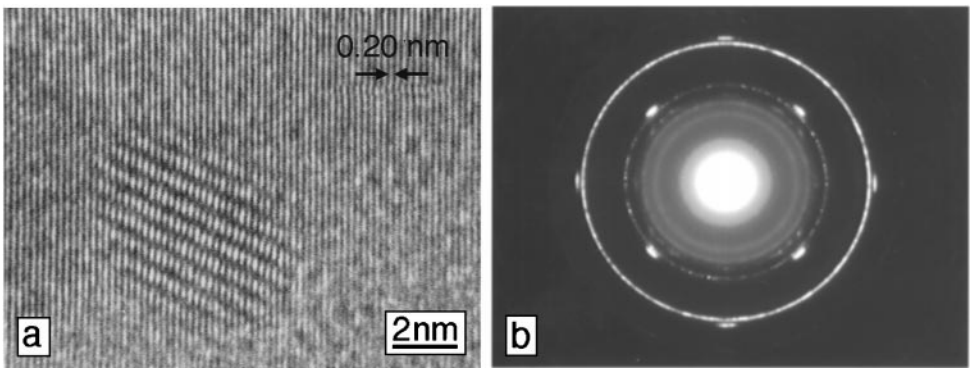

FIG. 4. Al_2O_3 crystallization induced by strong electron exposure: (a) HREM image showing alumina lattice plane fringes and Moiré fringes at the position of a Rh particle; (b) SAED pattern of a crystallized area: The diffraction spots originate from the epitaxial Rh particles while the rings are due to the (now) polycrystalline support.

by superposition of the patterns in Figs. 3b–h suggests that a complete characterization of all particle types has been obtained.

The distinct edges and corners of the Rh nanoparticles indicate that the bounding facets are well developed but a direct view of their surface structure is also desired. Some particles, e.g., the tetrahedra in (011) orientation, exhibit certain {111} and {001} surfaces parallel to the beam direction (perpendicular to the former NaCl substrate), and a profile of the surface structure of the edge-on facets can be recorded. Mainly smooth bounding faces and only a few {111} surface steps were observed. These steps originate from the growth process of the particles which probably proceeds via the formation of a new {111} layer on a complete {111} surface. Similar profile images were obtained from (011) cuboctahedra (44), but these are rather rare among Rh particles. The surface structure of facets inclined to the electron beam cannot be imaged in plane view, but the regular polyhedral shapes suggest that they are also rather smooth in the as-grown state.

3.2. *Annealing in High Vacuum*

To differentiate between the effect of thermal treatments and the changes on "reactive treatments" in O_2 and/or H_2, some of the as-prepared Rh/Al_2O_3 films were subjected to several annealing experiments in a vacuum of 1×10^{-5} Pa. No influence on either the metal particles or the support was detected up to 725 K.

3.3. *Structural Changes during Oxidizing and Reducing Treatments*

Changes of the support. In the as-prepared state the alumina films were amorphous and this provided a high image contrast between the metal particles and the surrounding support (Figs. 1 and 2). While heat treatments in oxygen or hydrogen up to 800 K did not change the support structure notably, electron irradiation more intense than that usually applied in electron microscopy induced crystallization of the alumina [this effect has also been reported by Heinemann and Poppa (45)]. A HREM image taken after strong electron exposure is shown in Fig. 4a. Alumina lattice fringes of 0.200 ± 0.004-nm spacing are resolved and Moiré fringes appear at the Rh particle due to double diffraction. To determine the structure of the now (poly-)crystalline support SAED patterns were recorded (Fig. 4b originates from a specimen area approx four times as large as Fig. 1a with an alumina grain size around 50 nm). The most intense (alumina) reflections indicated interplanar distances of 0.140, 0.197, 0.238, and 0.277 ± 0.004 nm. The best fit was obtained for γ- and for η-Al_2O_3 and the lattice fringes in Fig. 4a are therefore probably (400) planes. However, similar alumina modifications like δ cannot be excluded to appear as a small fraction. No preferred epitaxial relationship between the crystallized support and the metal particles was evident from SAED or HREM.

Oxidation. A survey of the effects of oxidation up to 725 K is presented in the CTEM images of Figs. 5a–d, and WBDF and HREM images of individual particles are shown in Figs. 6–9.

A mild oxidation up to 575 K (30 min) did not change the particle profiles on medium-magnification images (Fig. 5b) and no structural changes were monitored by SAED or WBDF. However, HREM images revealed a thin skin of oxide on the surface of many particles without a change in their morphology (Fig. 6a). The surface oxide, although already visible on the experimental image, is intensified by Fourier filtering. For that purpose the metal spots were masked by Bragg filters in the FFT (as already shown in Fig. 2b) and they were completely eliminated, while the spatial frequencies outside the selection were left unchanged. As a result, the metal contributions are removed from the image and only oxide lattice plane fringes appear in the filtered image. The oxidation seems to start at the particle edges, but more probably the thick metal core in the center of the

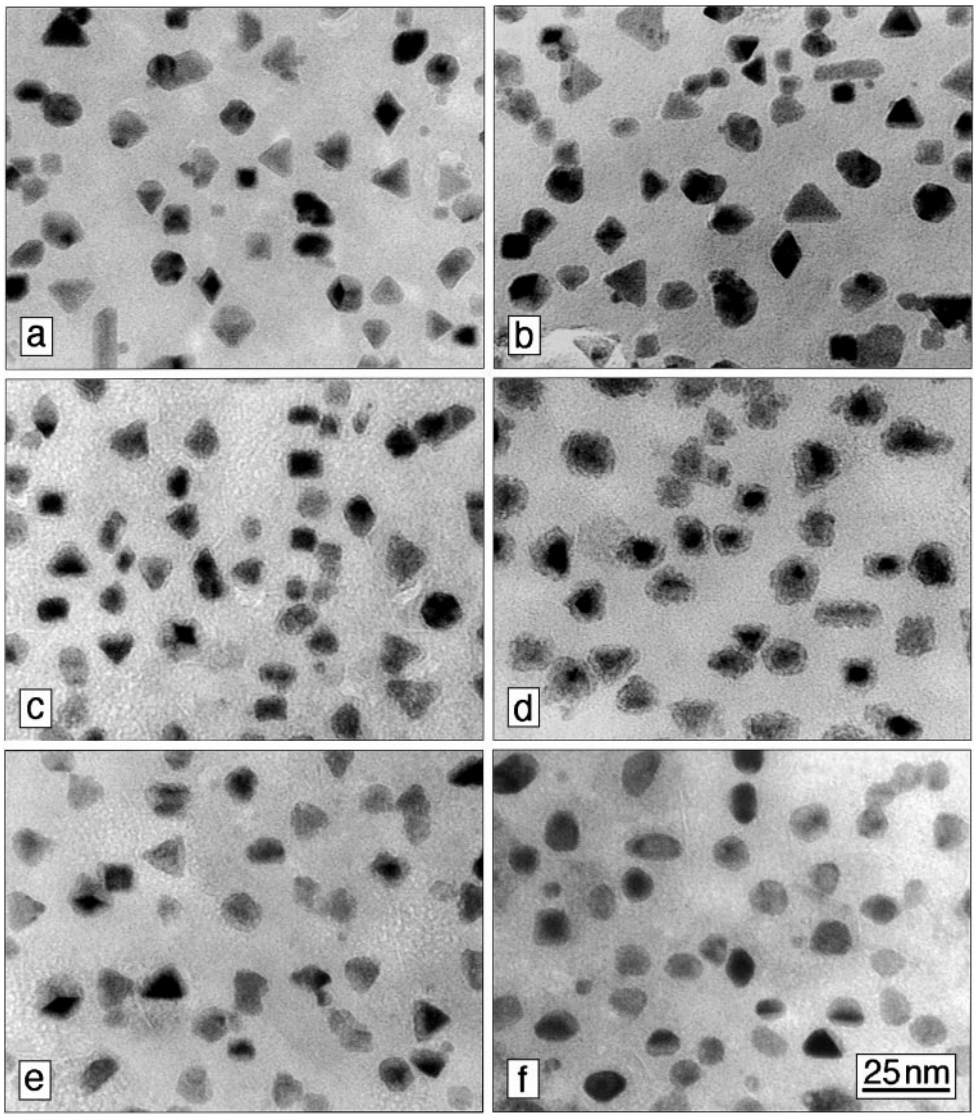

FIG. 5. CTEM images of a Rh/Al_2O_3 model catalyst with a mean particle size of 8.5 nm: (a) as-grown and on successive treatments in (b) O_2, 575 K, 30 min; (c) O_2, 675 K, 30 min; (d) O_2, 725 K, 120 min; (e) H_2, 525 K, 30 min; and (f) H_2, 725 K, 30 min.

particle prevents imaging of the total surface oxide by HREM. These results are in good agreement with other studies using (HR)TEM or X-ray photoelectron spectroscopy, which have also shown that the oxidation of Rh sets in at around 575 K (29, 33, 46). The oxidation has not been detected by SAED which gives integral information over a large number of particles (typically a few hundred), but is not surface sensitive and also insensitive against small local structural changes.

When the oxidation temperature was increased to 675–725 K (30 min) the surface oxide increased in thickness and was even visible on CTEM images as a roughening of the edges of the Rh particles (Fig. 5c; background features result from alumina crystallization during EM inspection). In addition, the SAED patterns exhibited weak oxide diffraction spots. The shape of the particles was still unchanged (see metal cores in Fig. 5c) and this was also revealed by WBDF images, which show, for instance, a distinct pyramidal metal core (Fig. 7b). On HREM images the oxide was again only imaged at the particle edges.

A model catalyst treated in O_2 at 725 K for 120 min is shown in Fig. 5d. Most particles had irregular outlines and consisted of a metal core surrounded by an oxide shell. Although distinct edges or corners were no longer visible, an epitaxial relationship between the metal core and the surface oxide was evident from SAED (Fig. 8b). The oxide spots are marked by arrows and originate from 0.155, 0.171, 0.233, and 0.260 ± 0.004-nm interplanar distances. Due to these spacings and the symmetry observed in electron diffraction, the oxide is hexagonal α-Rh_2O_3 and an

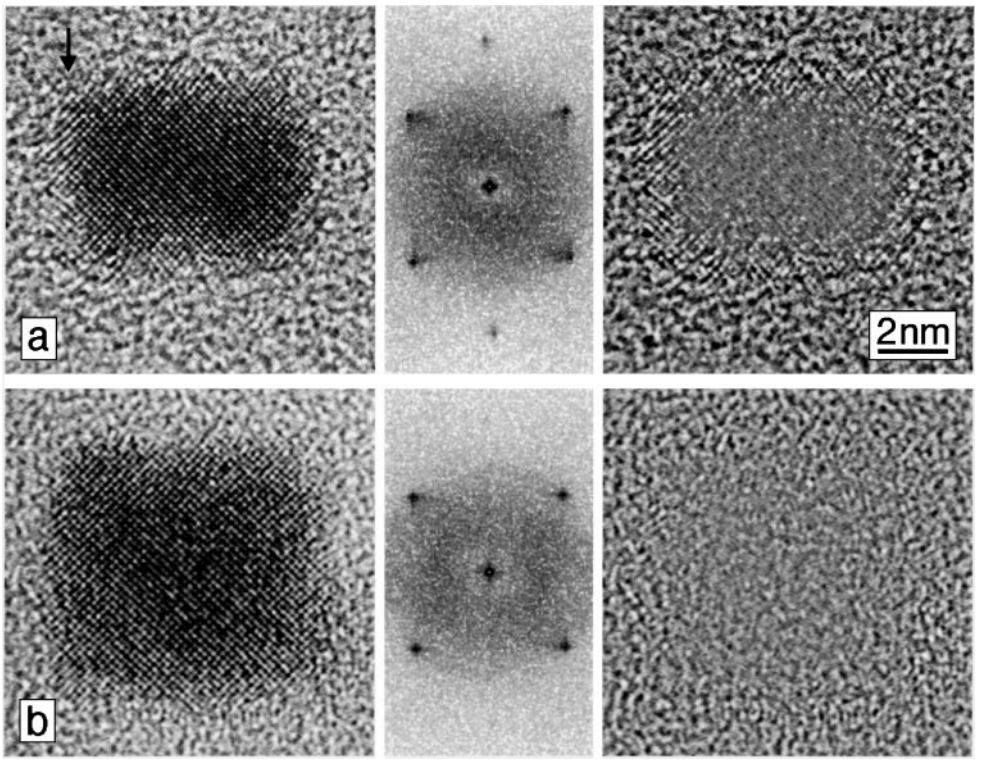

FIG. 6. HREM images (left), FFTs (center), and processed images (right) of (001)-oriented Rh particles after oxidation at 575 K, 30 min (a) and after subsequent low-temperature reduction at 525 K, 30 min (b). The thin oxide skin in (a) is illustrated by Fourier filtering.

epitaxial relationship of (035) $Rh_2O_3 \parallel$ (001) Rh, or more precisely [031] $Rh_2O_3 \parallel$ [001] Rh (zone axes), and [100] $Rh_2O_3 \parallel$ [110] Rh (crystallographic directions) was determined. The ordered growth of Rh_2O_3 on Rh was also reflected in HREM images, e.g., in Fig. 9a, where oxide lattice fringes of 0.26-nm spacing (d_{110}) are aligned nearly parallel to Rh {111} planes (spacing 0.22 nm). Fourier-filtering similar to that in Fig. 2 was applied to separate the image contributions of the metal and the oxide. If the intensities originating from the metal are masked in the FFT (marked by circles in Fig. 9b) and left unchanged while the rest of the power spectrum is partly suppressed, the visibility of the metal core is enhanced (Fig. 9c). If the oxide spots are masked, a complementary result is obtained (Fig. 9d). However, the epitaxial growth of Rh_2O_3 on (011)-oriented particles could not be eludicated clearly. No separation of metal and oxide could be achieved in dark field, and no topographical images were obtained because of the irregular shape of the particles and the small size of the metal cores.

It has been reported by Schmidt and co-workers (27, 29, 30) that the oxidation of Rh on alumina or silica proceeds via a particle breakup and that Rh_2O_3 spreads on these supports. However, Datye *et al.* (31–34) detected no breakup of Rh/SiO_2 on oxidation at 775 K and suggested the increase in particle size was due to the reduced density of the oxide ["volume increase" from Rh (102.9 g mol^{-1}, 12.4 g cm^{-3}) to $RhO_{1.5}$ (126.9 g mol^{-1}, 8.0 g cm^{-3})]. A complete oxidation of spherical Rh particles would therefore lead to a 24%

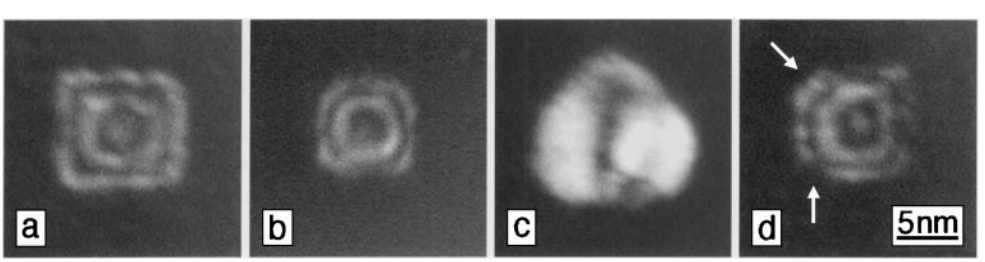

FIG. 7. (200) WBDF images of Rh nanoparticles: (a) as-grown and after heating in (b) O_2, 675 K, 30 min; (c) O_2, 725 K, 120 min followed by H_2, 525 K, 30 min; and (d) O_2, 725 K, 120 min followed by H_2, 525 K, 30 min and H_2, 725 K, 30 min.

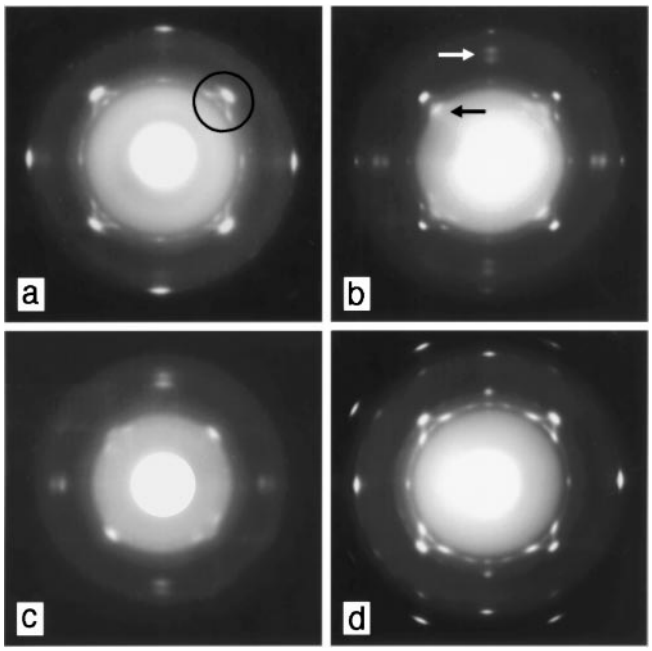

FIG. 8. Selected area electron diffraction patterns of epitaxially grown Rh/Al_2O_3 model catalysts: (a) as-prepared and after treatment in (b) O_2, 725 K, 120 min (oxide spots are marked by arrows); (c) O_2, 800 K, 120 min; and (d) O_2, 725 K, 120 min followed by H_2, 525 K, 30 min and H_2, 725 K, 30 min.

increase in diameter. Besides an hexagonal Rh_2O_3 phase, oxide lattice fringes of 0.29-nm spacing were found and Datye *et al*. suggested that they originate from a metastable cubic RhO phase (32, 33). Bernal *et al*. (12) studied the oxidation of ~5-nm Rh particles on a low-surface-area CeO_2 support but the precise structure of the oxide could not be unequivocally determined. The authors observed 0.26-nm spacings and favored α-Rh_2O_3 but could not exclude β-Rh_2O_3. Oxide spreading and subsequent metal redispersion were detected only on oxidation at 1173 K. These and our findings together with LEED studies of the low-pressure oxidation of Rh (111) (47, 48) indicate that the structure of a thin Rh surface oxide may differ from that of bulk Rh_2O_3. They also show that its wetting behavior is influenced by the method of the support preparation.

A distinct particle breakup was not observed in our experiments and no cracks could be detected in the particles on HREM images. One possible explanation is that the Rh particles investigated by Schmidt *et al*. were approximately two to three times larger than in this work and than in the studies of Datye *et al*. and Bernal *et al*. Smaller particles may accommodate oxide growth without cracks being formed. To examine whether a pronounced spreading of Rh_2O_3 on the support takes place, a Rh/Al_2O_3 model catalyst of 9.5-nm mean particle size was treated in oxygen at 800 K for 120 min. As evidenced by the SAED pattern in Fig. 8c, complete oxidation occurred. In good agreement with the model of Datye *et al*., the mean size of the particles had increased by 21% to 11.5 nm while no obvious wetting of the support was detected.

HREM image contrast calculations. As demonstrated in the previous subsection, the lattice fringe structure of particles in different states of oxidation can be directly imaged by HREM, but the micrographs have to be interpreted with care: After oxidation at 575 and 675 K the surface oxide seemed to be restricted to the particle edges (cf. Fig. 6a), but as already mentioned, the thick metal core probably prevented the detection of the entire oxide. An unambiguous explanation of these HREM images therefore requires the simulation of image contrast and a comparison between experimental and simulated images.

Based on the orientation relationship between metal and oxide (as revealed by SAED in Fig. 8b) a model structure of a Rh_2O_3 overlayer epitaxially oriented on a Rh layer was constructed by combining supercells of α-Rh_2O_3 and Rh (lateral size $\sim 2 \times 2$ nm, total thickness 2.5–7 nm). The simulations were carried out using the CrystalKit\McTempas and the Cerius^2 program packages with parameters according to the JEM 4000 EX (c_s 1.0 mm; focus spread 8.0 nm; beam divergence 0.6 mrad; objective lens aperture radius 7.0 nm^{-1}). The ratio between metal and oxide thicknesses was varied in a number of defocus series and three examples of simulated images are presented in Fig. 10. The calculations show that the oxide must be three to five times thicker than the metal to be discerned by HREM (Fig. 10a is identical to the simulated image of a pure Rh_2O_3 layer). Therefore, the oxide is detected only at the particle edges where the underlying metal is very thin.

At Rh_2O_3 : Rh ratios of 1 : 1 and below only the metal was imaged (Fig. 10c is nearly identical to the simulated image of a pure Rh layer; Fig. 10b is discussed below).

Reduction. Annealing of as-prepared Rh/Al_2O_3 films in H_2 between 525 and 625 K did not change the morphology of the Rh particles. Reduction at 725 K may lead to slightly rounded corners and to coalescence of closely neighbored particles, but generally no pronounced alterations were observed.

The oxidized model catalysts (cf. Oxidation) were subjected to reduction in H_2 at various temperatures, and in parallel, some specimens were reduced immediately after oxidation without removal from the microreactor and transfer to the electron microscope. No difference due to the repeated transfer between microreactor and electron microscope was observed.

Figure 6a shows a Rh half-octahedron after mild oxidation at 575 K, 30 min. As stated before, the thin oxide skin formed on the particle surface was visualized by Fourier filtering (or parts of it). LTR at 525 K, 30 min was sufficient to decompose the surface oxide without seriously changing the particle habit (Fig. 6b). Applying the Fourier filter routine of Fig. 6a to the HREM image of Fig. 6b shows that no oxide fringes are left in the processed image (not even at

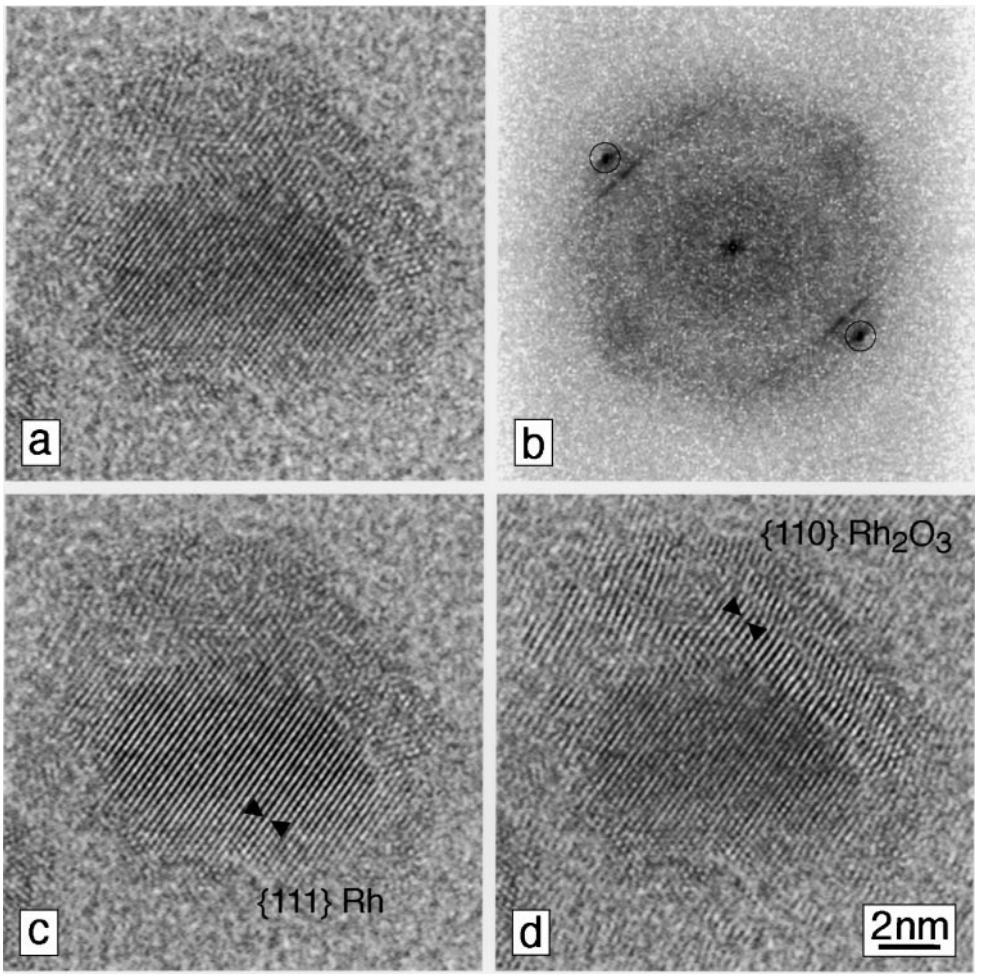

FIG. 9. (a) High-resolution electron image of a Rh model catalyst particle after oxidation at 725 K, 120 min; (b) FFT; (c, d) Fourier-filtered images to enhance the visibility of the metal core (c) and of the oxide shell (d).

the particle edges), indicating complete reduction. WBDF micrographs also confirmed that the as-grown habits were regained.

The effect of a low-temperature reduction on particles previously oxidized at 675–725 K was stronger, but almost independent of the degree of preoxidation (Fig. 5e). After LTR even particles having retained regular shapes after preoxidation (e.g., at 675 K; Fig. 5c) now exhibited rounded outlines or irregular profiles resulting from distinct truncations at the corners. While SAED indicated complete

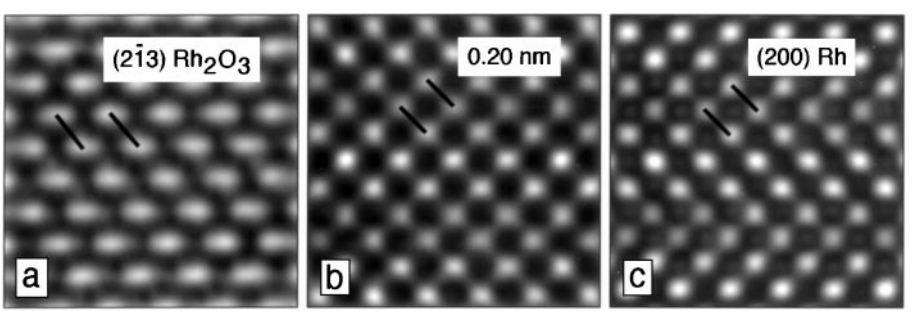

FIG. 10. HREM image contrast calculation of an α-Rh_2O_3 overlayer on Rh for different oxide-to-metal thickness ratios: (a) 5 : 1, (b) 2 : 1, (c) 1 : 1 (imaging parameters according to JEM 4000 EX, near Scherzer defocus).

reduction of the oxide to metal (pattern similar to Fig. 8d), the WBDF images revealed several different types of particles: Besides rounded pyramids (like in Fig. 7b) mainly particles of irregular shape or of a twinned or polycrystalline appearance were observed (Fig. 7c). Polycrystalline particles can be identified in dark field because, unlike bright field, only parts of them are imaged (different parts of the particle exhibit different zone axes). Such structures may not be easily characterized by SAED, but aggregates of small crystallites could be identified by Wong and McCabe (49) during the oxidation/reduction of Rh/SiO_2 using microbeam electron diffraction.

HREM images of the rounded pyramids were similar to that in Fig. 12a (and are not shown separately), and also, particles with irregular profiles exhibited mainly lattice plane fringes corresponding to Rh metal. However, in agreement with studies by Datye *et al*. (31, 32), it was found that for some (heavily oxidized) particles, a reduction temperature of 525 K is too low for a recrystallization into perfect metal crystallites. In Fig. 11a the disordered structure of a polycrystalline particle is presented. Rh {200} and {111} lattice plane fringes (0.190 and 0.220 nm) are observed in the particle center, while Rh {111} fringes and fringes of about 0.24-nm spacing appear at its periphery. One part of the particle exhibits no lattice resolution. Some other unusual particle shapes were observed: The particle in Fig. 11b is not a Rh half-octahedron as would be suggested from its appearance and from its symmetry in FFT because the measured lattice fringe distance is 0.24 nm and not 0.19 nm as expected for Rh {200}. According to the FFT, spacings of 0.18 nm are also evident. Interplanar distances of 0.24 and 0.18 nm do not arise from Rh_2O_3 and they do not arise from a particle tilt (this type of particle was too abundant to be explained by a simple tilt and it was never observed in as-grown samples). More likely, these spacings are due to interference effects resulting from the superposition of different crystalline materials which affect the image formation in the electron microscope: Annealing in O_2 up to 725 K had not completely oxidized the particles, but formed an oxide shell on the metal cores. When these uncompletely oxidized particles are reduced again, islands of metal are formed on top of the oxide (at the oxide–gas interface). Incomplete reduction will then result in rather complex sandwich structures like $Rh/Rh_2O_3/Rh$. This model is supported by simulated HREM images revealing that the combination of oxide and metal layers in a thickness ratio of 2 : 1 leads to fringe distances that cannot be attributed to either of these materials (Fig. 10b). The simulation of the sandwich structures is in progress (the supercells are complex because three layers in various orientations have to be modeled) and

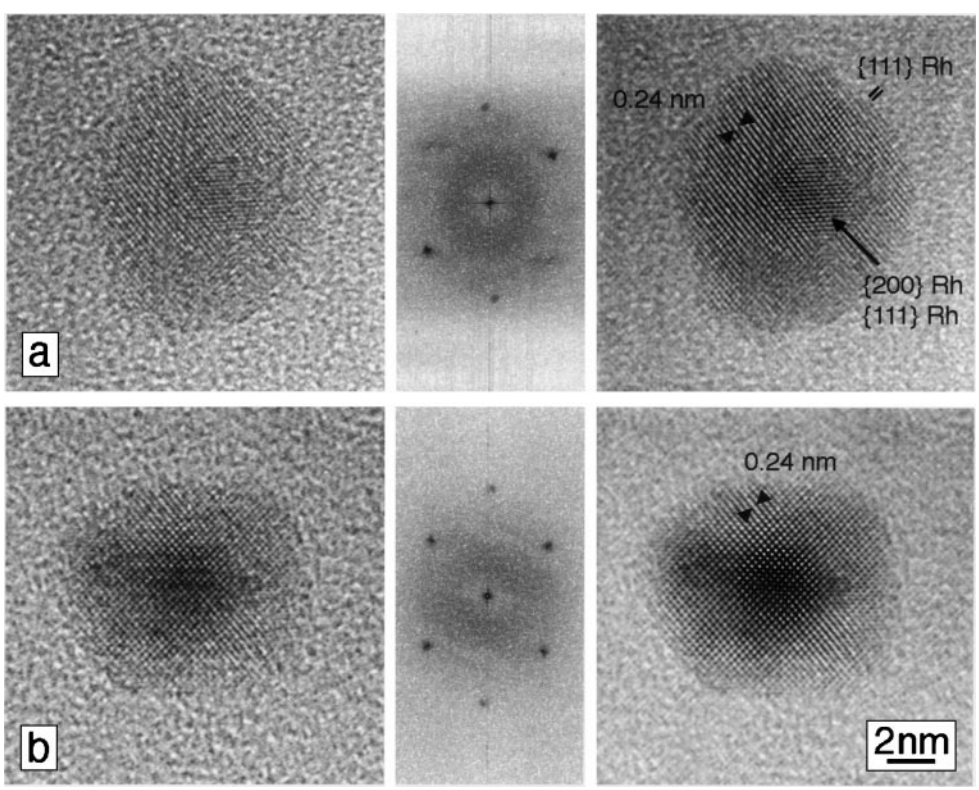

FIG. 11. Rh model catalyst particles after heating in O_2, 675 K, 30 min followed by low-temperature reduction in H_2 at 525 K, 30 min (see text): experimental HREM images (left), FFTs (center), and reconstructed images after background suppression (right).

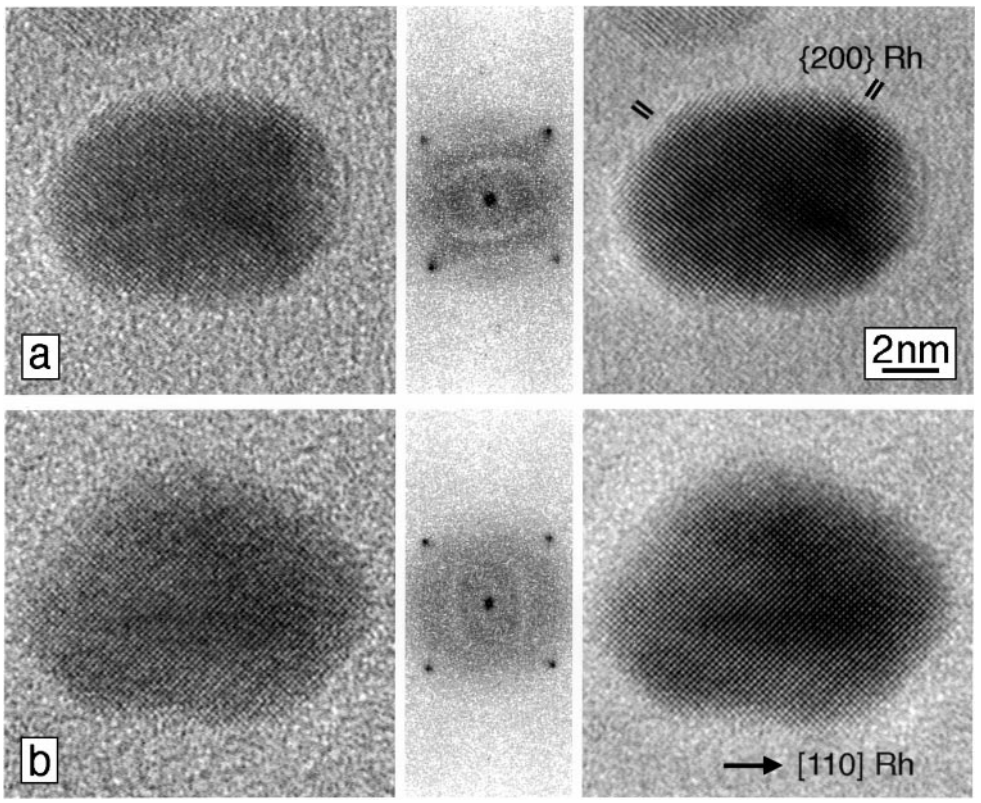

FIG. 12. A (001)-oriented half-octahedral (a) and a pseudopentagonal (b) Rh nanocrystal after oxidation in O_2, 725 K, 120 min followed by high-temperature reduction in H_2, 725 K, 30 min: Experimental HREM images (left), FFTs (center), and Fourier-filtered images (right).

preliminary results indicate that the observed fringe spacings of 0.24 nm may in fact result from a superposition of Rh and Rh_2O_3 (50). The observed effect is definitely not an imaging artifact due to crystallized alumina because, as shown in a previous subsection, crystalline Al_2O_3 is easily detected by HREM and SAED.

When Rh particles preoxidized at 675–725 K were subjected to HTR, the oxide shells were completely removed (Fig. 8d) but most particles now exhibited rounded profiles on medium-magnification images (Fig. 5f). According to WBDF imaging the original habits were perfectly reestablished. However, in most cases truncations at the corners were evident (see arrows in Fig. 7d) that lead to a rounded profile. HREM images conclusively proved a full recrystallization into nanocrystals on HTR since no polycrystalline particles or sandwich structures were detected (with the exception of the MTPs which had maintained their twinned structure during activation). A half-pyramidal crystallite and a pseudopentagonal crystallite are presented in Fig. 12. Although {110} or {111} truncations have been formed at the corners, distinct edges still exist and the original shapes can be easily identified. No significant increase in the number of surface steps was evident from profile images and coalescence occurred only when as-grown particles had been located closely together. An identical result was obtained when, after oxidation at 675–725 K and LTR, the model catalysts were subsequently reduced at high temperature.

4. DISCUSSION

To correlate the catalytic activity of the particles with their microstructure, three different steps of oxidation and reduction should be discussed: After oxidation at 675–725 K and subsequent LTR the turnover frequency in a number of hydrocarbon reactions (e.g., in the hydrogenolysis of *n*-pentane, neopentane, or *n*-butane) was found to be 5 to 10 times higher than after mild oxidation at 575 K and LTR or after oxidation at 675–725 K followed by HTR (25, 26, 31, 32). For the hydrogenolysis of ethane, even TOF changes up to 10^3 were reported (27, 28). These changes cannot be explained by alterations in the number of metal surface atoms as determined by electron microscopy and by hydrogen chemisorption. In Fig. 5 the metal surface area is about 24% of the total thin-film catalyst area during all activation stages (with the exception of Fig. 5d, which shows the strongly oxidized catalyst; surface area 30%). Also, the crystallite density of 3.5×10^{11} cm^{-2} and the mean particle size of 8.5 nm were nearly unchanged during all oxidation/reduction treatments. A pronounced sintering or redispersion (which would be an alternative explanation

of the observed TOF alterations) did not occur; therefore, the reactivity changes should result from surface structural changes of individual particles. This is further supported by the observation of Datye *et al.* (31) that no pretreatment-induced activity changes were found on Rh particles <1 nm, presumably because their small size did not permit pronounced changes of the surface structure.

On mild oxidation at 575 K and subsequent LTR the initial habit of most particles was reestablished. The nanocrystals exhibited mainly low-index surfaces with a limited number of surface steps, i.e., preferentially high-coordinated sites.

After oxidation at 675–725 K followed by LTR most particles had irregular outlines, which indicate the presence of high-index facets or low-coordinated sites. HREM revealed that in the most active state the structure of the particles may be highly disordered; e.g., the polycrystalline Rh particles consist of small crystalline domains, exposing mainly high-index facets. In addition, an incomplete reduction of incompletely oxidized particles resulted in $Rh/Rh_2O_3/Rh$ sandwich structures. If some surface oxide is left after LTR, an *in situ* reduction under reaction conditions will also produce disordered surface structures because the reaction temperatures are too low to allow full recrystallization.

After oxidation at 675–725 K and HTR the particles regained their initial shapes and therefore exposed mainly low-index surface facets. Although truncations of corners were frequent, profile images of half-tetrahedra did not indicate a considerable increase in the number of surface steps.

Our results, obtained on small supported particles, agree well with single-crystal studies in ultrahigh-vacuum high-pressure cells indicating that smooth, low-Miller-index close-packed surfaces generally exhibit reduced (hydrogenolysis) reactivity in comparison to stepped high-index facets and, therefore, they may help to link the two model systems (31, 32, 51). However, there is some disagreement with related studies on small particles. Under our experimental conditions, we did not observe a considerable spreading of Rh oxide on the support or a particle breakup as reported by Schmidt and co-workers (27, 29, 30). The metal crystallites oxidized uniformly without forming any voids or cracks. No intraparticle redispersion was observed after oxidation at 775 K and at reduction temperatures between 325 and 525 K. The reason for this difference may be that our particles were, at least in part, embedded in the support. This may prevent an easy oxide spreading, which is a prerequisite for redispersion. Our findings are in better agreement with those of Datye *et al.* (31–34). They investigated the oxidation of 5-nm Rh particles and also observed an oriented overgrowth of the oxide on the metal. On reduction, Datye *et al.* observed a restructuring of the Rh crystals to polycrystalline particles but also to particles with an amorphous core, possibly of unreduced oxide (35). This observation indicates again that the reduction starts at the surface of the particles and it supports the model of sandwich structures.

5. CONCLUSIONS

The catalytic performance of alumina-supported Rh depends sensitively on the surface structure of the metal nanoparticles. As long as the regular polyhedral habit of the Rh particles was retained or regained, i.e., as long as mainly low-index facets were exposed, the activity of the model catalysts was only moderate. However, an activity maximum was observed after preoxidation at 675–725 K and LTR, which resulted in the formation of faceted and polycrystalline Rh particles and presumably in the formation of complex sandwich structures. While high-coordination sites dominate on low-index faces [e.g., C_9 according to (52)], the polycrystalline particles consist of smaller crystalline domains and expose mainly low-coordinated sites (i.e., their surface is considerably roughened). The observed increased activity of low-coordination sites is in good agreement with studies performed on flat, stepped, and kinked noble metal single-crystal surfaces in a series of alkane hydrogenolysis reactions where maximum rates were obtained on surfaces containing high concentrations of steps and kinks (31, 32, 51). On the other hand, it is known from temperature-programmed desorption that these sites exhibit the highest heats of adsorption and are therefore unfavorable for rapid reaction turnovers (53). Consequently, following a suggestion by Somorjai (54, 55) it can be assumed that the adsorption of a reactant molecule may rearrange the metal surface near a step ("adsorbate-induced restructuring") and may thereby create the suitable configuration for bond breaking.

ACKNOWLEDGMENTS

The authors thank R. Tessadri and E. Mersdorf (University of Innsbruck) for assistance in the elemental analysis of thin films. Helpful discussions with W. Neumann (HU Berlin) and D. Timpel (MPI Halle) are gratefully acknowledged. G.R. is indebted to the Max Planck Society for a SC fellowship and to the members of the MPI Halle for their hospitality.

REFERENCES

1. Bond, G. C., *J. Mol. Catal.* **81**, 99 (1993).
2. Sushumna, I., and Ruckenstein, E., *J. Catal.* **108**, 77 (1987).
3. Wang, T., Lee, C., and Schmidt, L. D., *Surf. Sci.* **163**, 181 (1985).
4. Smith, D. J., White, D., Baird, T., and Fryer, J. R., *J. Catal.* **81**, 107 (1983).
5. Glassl, H., Kramer, R., and Hayek, K., *J. Catal.* **68**, 388 (1981).
6. Chapon, C., Henry, C. R., and Chemam, A., *Surf. Sci.* **162**, 747 (1985).
7. Jacobs, J. W. M., and Schryvers, D., *J. Catal.* **103**, 436 (1987).
8. Datye, A. K., Logan, A. D., Blankenburg, K. J., and Smith, D. J., *Ultramicroscopy* **34**, 47 (1990).
9. Ramachandran, A. S., Anderson, S. L., and Datye, A. K., *Ultramicroscopy* **51**, 282 (1993).
10. Jefferson, D. A., and Harris, P. J. F., *Nature* **332**, 617 (1988).
11. Harris, P. J. F., *J. Catal.* **97**, 527 (1986).

12. Bernal, S., Botana, F. J., Calvino, J. J., Cifredo, G. A., Pérez-Omil, J. A., and Pintado, J. M., *Catal. Today* **23**, 219 (1995).
13. Gunter, P. L. J., Niemantsverdriet, J. W. H., Ribeiro, F. H., and Somorjai, G. A., *Catal. Rev. Sci. Eng.* **39**, 77 (1997).
14. Datye, A. K., and Smith, D. J., *Catal. Rev. Sci. Eng.* **34**, 129 (1992).
15. José-Yacamán, M., and Avalos-Borja, M., *Catal. Rev. Sci. Eng.* **34**, 55 (1992).
16. Smith, D. J., and Marks, L. D., *Ultramicroscopy* **16**, 101 (1985).
17. Smith, D. J., Petford-Long, A. K., Wallenberg, L. R., and Bovin, J.-O., *Science* **233**, 872 (1986).
18. Singh, A. K., Pande, N. K., and Bell, A. T., *J. Catal.* **94**, 422 (1985).
19. Braunschweig, E. J., Logan, A. D., Datye, A. K., and Smith, D. J., *J. Catal.* **118**, 227 (1989).
20. Rupprechter, G., Hayek, K., Rendón, L., and José-Yacamán, M., *Thin Solid Films* **260**, 148 (1995).
21. Hayek, K., *J. Mol. Catal.* **51**, 347 (1989).
22. Gehrer, E., and Hayek, K., *J. Mol. Catal.* **39**, 293 (1987).
23. Zimmermann, C., and Hayek, K., *in* "New Frontiers in Catalysis" (L. Guczi *et al*., Eds.), Proc. 10th Int. Congr. Catal., p. 2375. Elsevier, Budapest, 1992.
24. Zimmermann, C., and Hayek, K., *Chem. Ing. Tech.* **63**, 68 (1991).
25. Rupprechter, G., Ph.D. thesis 1996, Leopold-Franzens-Universität, Innsbruck, Austria.
26. Rupprechter, G., Seeber, G., Goller, H., and Hayek, K., in preparation.
27. Schmidt, L. D., and Krause, K. R., *Catal. Today* **12**, 269 (1992).
28. Gao, S., and Schmidt, L. D., *J. Catal.* **115**, 356 (1989).
29. Burkhardt, J., and Schmidt, L. D., *J. Catal.* **116**, 240 (1989).
30. Wang, T., and Schmidt, L. D., *J. Catal.* **70**, 187 (1981).
31. Kalakkad, D., Anderson, S. L., Logan, A. D., Peña, J., Braunschweig, E. J., Peden, C. H. F., and Datye, A. K., *J. Phys. Chem.* **97**, 1437 (1993).
32. Logan, A. D., Sharoudi, K. S., and Datye, A. K., *J. Phys. Chem.* **95**, 5568 (1991).
33. Logan, A. D., Braunschweig, E. J., Datye, A. K., and Smith, D. J., *Ultramicroscopy* **31**, 132 (1989).
34. Chakraborti, S., Datye, A. K., and Long, N. J., *J. Catal.* **108**, 444 (1987).
35. Braunschweig, E. J., Logan, A. D., Chakraborti, S., and Datye, A. K., *in* "Catalysis: Theory to Practice" (M. J. Phillips and M. Ternan, Eds.), Proc. 9th Int. Congr. Catal., Vol. 3, p. 1122. Chem. Inst. of Canada, Ottawa, 1988.
36. Rupprechter, G., Seeber, G., Hayek, K., and Hofmeister, H., *Phys. Status Solidi A* **146**, 449 (1994).
37. José-Yacamán, M., Díaz, G., and Gómez, A., *Catal. Today* **23**, 161 (1995).
38. Gillet, M., and Renou, A., *Surf. Sci.* **90**, 91 (1979).
39. Henry, C. R., Chapon, C., Duriez, C., and Giorgio, S., *Surf. Sci.* **253**, 177 (1991).
40. Hofmeister, H., Haefke, H., and Krohn, M., *J. Cryst. Growth* **58**, 507 (1982).
41. Gillet, M. F., and Channakhone, S., *J. Catal.* **97**, 427 (1986).
42. Rupprechter, G., Hayek, K., and Hofmeister, H., *Vacuum* **46**, 1035 (1995).
43. Robinson, F., and Gillet, M., *Thin Solid Films* **98**, 179 (1982).
44. Rupprechter, G., Hayek, K., and Hofmeister, H., *in* "Electron Microscopy 1996" (D. Cottell and M. Steer, Eds.), Proc. 11th Eur. Congr. Electron Microsc., Vol. 1, m/m3. UCD Belfield, Dublin, 1996.
45. Heinemann, K., and Poppa, H., *Ultramicroscopy* **17**, 213 (1985).
46. Koshy, J., *Thin Solid Films* **51**, L17 (1978).
47. Logan, A. D., Datye, A. K., and Houston, J. E., *Surf. Sci.* **245**, 280 (1991).
48. Castner, D. G., and Somorjai, G. A., *Appl. Surf. Sci.* **6**, 29 (1980).
49. Wong, C., and McCabe, R. W., *J. Catal.* **107**, 535 (1987).
50. Rupprechter, G., Hayek, K., and Hofmeister, H., in preparation.
51. Davis, S. M., Zaera, F., and Somorjai, G. A., *J. Am. Chem. Soc.* **104**, 7453 (1982).
52. Van Hardeveld, R., and Hartog, F., *Surf. Sci.* **15**, 189 (1969).
53. Somorjai, G. A., *Surf. Sci.* **299/300**, 849 (1994).
54. Somorjai, G. A., *J. Mol. Catal. A* **107**, 39 (1996).
55. Somorjai, G. A., and Rupprechter, G., *in* "Dynamics of Surfaces and Reaction Kinetics in Heterogeneous Catalysis" (G. F. Froment and K. C. Waugh, Eds.), Studies in Surface Science and Catalysis, Vol. 109, p. 35. Elsevier, Amsterdam, 1997.